

Sample dispersion in isotachophoresis

G. GARCIA-SCHWARZ¹, M. BERCOVICI², L. A. MARSHALL³
AND J. G. SANTIAGO^{1†}

¹Department of Mechanical Engineering, Stanford University, Stanford, CA 94305, USA

²Department of Aeronautics and Astronautics, Stanford University, Stanford, CA 94305, USA

³Department of Chemical Engineering, Stanford University, Stanford, CA 94305, USA

(Received 29 October 2010; revised 27 January 2011; accepted 14 March 2011;
first published online 12 May 2011)

We present an analytical, numerical and experimental study of advective dispersion in isotachophoresis (ITP). We analyse the dynamics of the concentration field of a focused analyte in peak mode ITP. The analyte distribution is subject to electromigration, diffusion and advective dispersion. Advective dispersion results from strong internal pressure gradients caused by non-uniform electro-osmotic flow (EOF). Analyte dispersion strongly affects the sensitivity and resolution of ITP-based assays. We perform axisymmetric time-dependent numerical simulations of fluid flow, diffusion and electromigration. We find that analyte properties contribute greatly to dispersion in ITP. Analytes with mobility values near those of the trailing (TE) or leading electrolyte (LE) show greater penetration into the TE or LE, respectively. Local pressure gradients in the TE and LE then locally disperse these zones of analyte penetration. Based on these observations, we develop a one-dimensional analytical model of the focused sample zone. We treat the LE, TE and LE–TE interface regions separately and, in each, assume a local Taylor–Aris-type effective dispersion coefficient. We also performed well-controlled experiments in circular capillaries, which we use to validate our simulations and analytical model. Our model allows for fast and accurate prediction of the area-averaged sample distribution based on known parameters including species mobilities, EO mobility, applied current density and channel dimensions. This model elucidates the fundamental mechanisms underlying analyte advective dispersion in ITP and can be used to optimize detector placement in detection-based assays.

Key words: MHD and electrohydrodynamics, microfluidics

1. Introduction

Isotachophoresis (ITP) is a well-established electrophoretic separation and focusing technique used for sample preconcentration and analysis in a wide range of chemical and biological applications (Gebauer, Malá & Boček 2007). In ITP, sample ions focus between leading (LE) and trailing electrolytes (TE) with respectively higher and lower effective ion mobility. ITP leverages sharp gradients in electric field established by applying voltage to a heterogenous buffer system. These gradients create self-sharpening interfaces which typically migrate at a constant velocity. For fully ionized species (strong electrolytes), maximum achievable analyte concentration is governed by

† Email address for correspondence: juan.santiago@stanford.edu

the Kohlrausch regulating function (KRF) (Kohlrausch 1897). For buffer chemistries using (partially ionized) weak electrolytes, the maximum analyte concentration is ruled by the Jovin and Alberty relations (Alberty 1950; Jovin 1973). Analytes can focus in two modalities depending on initial analyte concentration as well as focusing rate and time. High initial analyte concentrations and sufficient focusing time result in 'plateau mode', which is characterized by distinct analyte zones each at a locally uniform concentration determined generally by the Jovin and Alberty relations (Alberty 1950; Martin & Everaerts 1970; Jovin 1973). In contrast, sufficiently low initial analyte concentrations lead to 'peak mode' focusing where sample ions accumulate in a sharp peak between neighbouring species (e.g. between the LE and TE if no other plateau mode species are present). Peak mode analytes do not typically significantly contribute to local conductivity (Chen *et al.* 2005). In this latter modality, peak widths are determined in part by the thickness of the dispersed boundary between adjoining species. For all analytes in peak mode, dispersion of the LE–TE interface and the electrophoretic focusing dynamics of the analyte itself each contribute to the shape and width of the analyte distribution.

The study of the diffusive LE–TE boundary has received significant attention as it plays an important role in determining the sensitivity (and sometimes resolution) of ITP (for a discussion of ITP sensitivity *versus* resolution, see Khurana & Santiago 2008). An analytical derivation of this boundary's characteristic width was first presented by MacInnes & Longworth (1932) who modelled ITP as a one-dimensional balance of diffusion and electromigration. Similar derivations were later provided as part of the analytical and experimental work of Konstantinov & Oshurkova (1966) and the numerical work of Saville (1990). However, the aforementioned studies neglected the effect of convective dispersion due to non-uniform electro-osmotic flow (EOF). In the presence of finite wall zeta potentials, axially non-uniform electro-osmotic (EO) slip velocities give rise to internal pressure gradients that disperse ITP interfaces. Dispersion has been shown to significantly decrease the sensitivity and resolution of ITP-based assays (Bharadwaj *et al.* 2008; Khurana & Santiago 2008).

To our knowledge, Konstantinov & Oshurkova (1966) were the first to explore the effect of convective dispersion on ion concentration fields in ITP. They studied dispersion due to uniform pressure-driven flow and suggested a simple heuristic relation between the area-averaged interface width and the magnitude of the uniform pressure gradient. Saville (1990) later presented an analytical derivation for the same case, where dispersion is due solely to an externally imposed and uniform parabolic flow. Khurana & Santiago (2008) modelled ITP dispersion as a balance between axial convection/diffusion and transverse (e.g. radial) electromigration. They presented a semi-empirical scaling relationship for the effective dispersion coefficient at the interface that yields improved agreement with experiments compared to Saville's model. Recently, Schönfeld *et al.* (2009) developed a two-dimensional translationally invariant numerical simulation of ITP that couples the mass transport and incompressible flow equations to account for non-uniform EOF. They posed a simple heuristic scaling wherein the ITP interface width is proportional to the difference between the LE and TE slip velocities as well as to the characteristic radial diffusion time. They verified this scaling with their simulations. They also present experimental visualizations of a focused fluorescent species showing pronounced curvature in the transverse direction due to non-uniform EOF.

Despite these advancements, all flow analyses and numerical models have so far focused on dispersion of the diffuse LE–TE boundary. We know of no models for the distribution of a focused and dispersed analyte which takes into account the analyte's

physical properties. In particular, the important role of species mobility and its value relative to the TE and LE ion mobilities has not been explored. All dispersion models have also neglected the effects of electrohydrodynamic body forces associated with the coupling of conductivity gradients and diffusion at ITP interfaces. Such coupling creates regions of net free charge in the bulk liquid (outside the electric double layer) that can modify electrokinetic flow and lead to instabilities (Lin *et al.* 2004; Chen *et al.* 2005; Sounart & Baygents 2007; Santos & Storey 2008; Persat & Santiago 2009).

In this work we describe numerical, analytical and experimental studies of analyte dispersion dynamics in peak mode ITP. We develop an axisymmetric numerical simulation which accounts for non-uniform EOF, the mobility and diffusivity of the focused species in peak mode, and electric body forces. We use this simulation to show that the value of the analyte mobility relative to the TE and LE mobilities can have a dramatic effect on the shape and width of the analyte distribution. As we shall see, this effect can lead to significant electromigration-based dispersion of the analyte peak even in the absence of non-uniform EOF. This mobility effect can also strongly couple with advective dispersion to further broaden the sample distribution. We propose a heuristic analytical model for analyte dispersion dynamics where the analyte characteristic width is dominated by local Taylor–Aris-type dispersion (Taylor 1953; Aris 1956). This leads to a closed-form area-averaged model that, for the first time, enables detailed predictions of dispersed sample distributions in ITP and accounts for the specific ion mobilities of the TE, LE and analyte species. We conclude by validating and exploring the limits of our model and simulations with a set of controlled experiments including repeatable quantitative concentration field measurements under a variety of conditions.

2. ITP dispersion due to EOF

In microfluidic systems with channels of order $10\mu\text{m}$ or larger, EOF is often modelled using a simple slip velocity condition known as the Helmholtz–Smoluchowski equation (Probstein 1994). This boundary condition provides a linear relationship between EO slip and local applied electric field and can be applied to flows with non-uniform conductivities (Santiago 2001). In ITP, a current applied through axial conductivity gradients creates electric field gradients that lead to analyte focusing. The electric field is uniform within both the LE and the TE, and its value in each zone can be related through the ITP condition, $\mu_{LE}E_{LE} = \mu_{TE}E_{TE}$ (Everaerts, Beckers & Verheggen 1976). Axial variation of the electric field also causes non-uniform EO slip velocities, depicted in figure 1, which in turn generate internal pressure gradients. Far from the LE–TE interface, local pressure gradients are uniform and proportional to the difference between local and axial-average EO velocities (Anderson & Idol 1985; Herr *et al.* 2000; Ghosal 2002). An adverse pressure gradient (relative to bulk flow) forms in the TE where the EO slip is typically higher than the axial-average EOF, and a favourable pressure gradient forms in the LE where the EO slip is typically lower than the axial-average EOF.

Figure 1 describes some of the main features of ITP boundaries dispersed by non-uniform EOF. Throughout this paper, we will assume negative EO mobility (typical for glass or silica for approximately pH 4 and above, see Kirby & Hasselbrink 2004) and anionic ITP, but the concepts are easily extended to cover cationic ITP and/or positive wall charge. Near the beginning of a typical ITP experiment, the high-conductivity LE fills most of the channel so that the axial-average EOF is dominated by the EO slip in the LE zone. In this case, the mismatch between the local EO slip velocity and

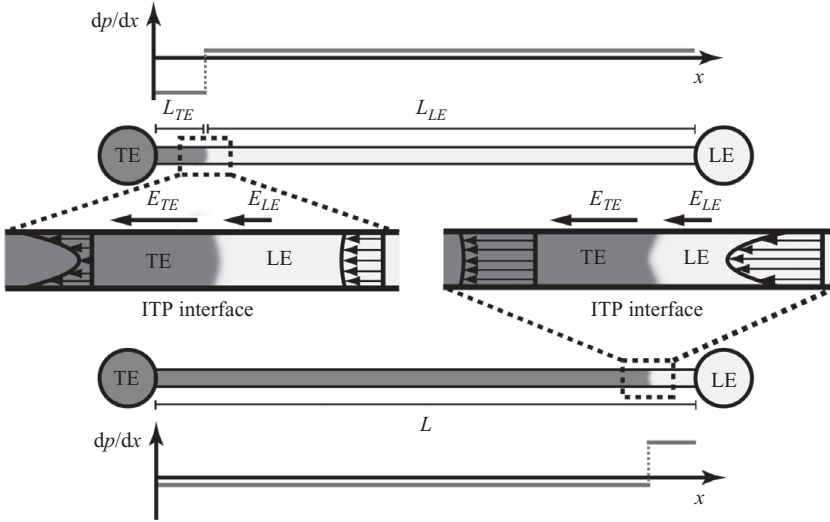


FIGURE 1. Schematic showing the curvature of the LE–TE interface at two locations along a channel. The parameters L_{TE} and L_{LE} represent the lengths of the TE and LE zones, respectively ($L = L_{TE} + L_{LE}$ is the total length of the channel). Arrow lengths (outside magnified channel) denote the relative strength of the local electric field in the LE and TE. An axially non-uniform electric field leads to non-uniform EO slip velocities which, in turn, result in the formation of favourable and adverse pressure gradients within the LE and TE zones, respectively. The magnitude of these opposing pressure gradients, given analytically in (2.1a and 2.1b), is governed by the difference between local and axial-average EO velocities (Anderson & Idol 1985; Herr *et al.* 2000; Ghosal 2002) and determines the shape of the LE–TE interface. For $L_{TE}/L < 0.5$, the TE pressure gradient is larger than that of the LE, and *vice versa* for $L_{TE}/L > 0.5$. The detailed views labelled ‘ITP interface’ are scalar fields of LE concentration in the capillary mid-plane taken from the numerical simulations described in § 3.

the axial-average EO velocity is small within the LE and large within the shorter TE zone. As the experiment progresses, the low-conductivity TE fills more of the channel and increases the axial-average EO velocity. Accordingly, the LE pressure gradient increases as the TE pressure gradient decreases. The local pressure gradients within the LE and TE zones (sufficiently far from the LE–TE interface) can be expressed analytically as

$$\left. \frac{\partial p}{\partial z} \right|_{TE} = -\frac{8\eta}{R^2} E_{LE} (\mu_{EOF}^{LE} - \gamma \mu_{EOF}^{TE}) \left(1 - \frac{L_{TE}}{L} \right), \quad (2.1a)$$

$$\left. \frac{\partial p}{\partial z} \right|_{LE} = \frac{8\eta}{R^2} E_{LE} (\mu_{EOF}^{LE} - \gamma \mu_{EOF}^{TE}) \left(\frac{L_{TE}}{L} \right). \quad (2.1b)$$

Here, η is the dynamic viscosity, R is the channel radius, μ_{EOF}^{LE} and μ_{EOF}^{TE} are the respective wall mobilities in the LE and TE, γ is the ratio of LE to TE electrophoretic mobility ($\gamma \equiv \mu_{LE}/\mu_{TE}$, where $\gamma > 1$), E_{LE} is the electric field in the LE, L_{TE} is the axial length of the TE zone and L is the total channel length. We give a detailed derivation of this result in Appendix A of the supplementary material available at journals.cambridge.org/flm. The relative magnitude of the LE and TE pressure gradients determines, in part, the direction of curvature of the LE–TE interface (see figure 1). When the channel is mostly filled with LE, the interface shows curvature associated with a strong adverse pressure gradient. In contrast, when the channel

is mostly filled with TE, the interface shows curvature associated with a strongly favourable pressure gradient. The detailed views showing ‘ITP interface’ scalar fields in figure 1 are results from numerical simulations presented in § 3.

EOF also affects the velocity of ITP zones. The axial-average EOF velocity (\bar{U}_{EOF}) acts against anion electromigration and thus results in a reduced zone velocity, U_{zone} . This adjusted zone velocity depends on values of EO mobility in the TE and LE as well as the axial position of the LE–TE interface. The adjusted velocity, $U_{zone} = U_{ITP} + \bar{U}_{EOF}$, can be expressed as

$$U_{zone} = \mu_{LE} E_{LE} + \left[\left(\frac{L_{TE}}{L} \right) \mu_{EOF}^{TE} E_{TE} + \left(1 - \frac{L_{TE}}{L} \right) \mu_{EOF}^{LE} E_{LE} \right]. \quad (2.2)$$

Here $U_{ITP} \equiv \mu_{LE} E_{LE}$ is the ITP velocity in the absence of EOF, μ_{LE} is the LE electrophoretic mobility and E_{TE} is the electric field in the TE. The interplay of electrophoresis and EOF can have drastic effects on ITP. For example, the sample zone will not enter the channel from the TE reservoir if the EO mobility in the LE is greater than the LE electrophoretic mobility ($\mu_{EOF}^{LE} > \mu_{LE}$). When instead the EO mobility in the TE is greater than the LE electrophoretic mobility ($\mu_{EOF}^{TE} > \mu_{LE}$), the sample zone eventually becomes stationary within the channel where the bulk flow velocity exactly counterbalances the ITP velocity ($\bar{U}_{EOF} = -U_{ITP}$). Under the latter condition, the sample zone can also enter the channel from the LE reservoir (for the case where the channel is initially filled entirely with TE).

3. Numerical simulations of dispersion in ITP

3.1. Governing equations and boundary conditions

In this section we present the governing equations for our numerical model of ITP. We assume that all species are dilute and monovalent. We define the total concentration, c_i , of a monovalent species i as

$$c_i = c_{i,0} + c_{i,\pm 1}, \quad (3.1)$$

where $c_{i,0}$ is the concentration of its neutral form and $c_{i,\pm 1}$ is the concentration of its ionized form (with valence of +1 or −1). We define the effective mobility of the i th species as

$$\mu_i = \left(\frac{c_{i,\pm 1}}{c_i} \right) \mu_{i,\pm 1}, \quad (3.2)$$

where $\mu_{i,\pm 1}$ is the corresponding fully ionized mobility. With these conventions and simplifications, the general convective-diffusion equation governing transport of the LE, TE, counter-ion and analyte through electromigration, diffusion and convection is

$$\frac{\partial c_i}{\partial t} + \nabla \cdot [\mathbf{u}c_i + z_i \mu_i \mathbf{E}c_i - D_i \nabla c_i] = 0 \quad \text{for } i = \text{LE, TE, CI, A}. \quad (3.3)$$

Here c_i is the total concentration of the i th species, \mathbf{u} is the fluid velocity field, z_i is the valence of the i th species, μ_i is the effective electrophoretic mobility of the i th species, D_i is the diffusivity of the i th species and \mathbf{E} is the electric field. In general $\mathbf{E} = -\nabla\phi$, where ϕ is the electric potential. The subscripts CI and A refer respectively to the counter-ion (here a cation) and the focused analyte ion. We use the Nernst–Einstein equation to relate ion diffusivity to electrophoretic mobility, $D_i = \mu_{i,\pm 1} R_\mu T / F$, where R_μ is the gas constant, T is the temperature in kelvin and F is Faraday’s constant.

The fluid velocity and pressure are governed by the low-Reynolds-number Stokes equations with an electric body force,

$$\nabla p = \eta \nabla^2 \mathbf{u} + [\epsilon \nabla \cdot \mathbf{E}] \mathbf{E}, \quad (3.4)$$

$$\nabla \cdot \mathbf{u} = 0. \quad (3.5)$$

Here p is the pressure and ϵ is the electrolyte permittivity. The final term in the momentum equations represents the electric body force, which accounts for a force exerted on the fluid by regions of net free charge moving under the influence of an electric field. In our domain of interest, this net charge resides in the bulk liquid (outside the electric double layer) and is associated with the coupling of electric field and conductivity gradients (see Lin *et al.* 2004 for further discussion). We assume constant permittivity and extract ϵ from the divergence operator.

The electric potential is governed by the conservation of charge,

$$\frac{\partial \rho_e}{\partial t} + \nabla \cdot \mathbf{j} = 0, \quad (3.6)$$

where

$$\mathbf{j} = F \left[\mathbf{E} \sum_i z_i \mu_{i,z_i} c_{i,z_i} + \mathbf{u} \sum_i z_i c_{i,z_i} - \sum_i z_i D_i \nabla c_{i,z_i} \right]. \quad (3.7)$$

Here ρ_e is the free charge density and \mathbf{j} is the current density, which includes conductive, convective and diffusive components.

As mentioned above, conductivity gradients in ITP lead to distributions of net charge in the bulk liquid. However, as discussed by Saville & Palusinski (1986), in ITP the characteristic length scale of the conductivity interface is typically much larger than the electric length scale associated with regions of significant net charge (i.e. much larger than the Debye length). We can therefore invoke the electroneutrality approximation and neglect the unsteady and convective terms in (3.6). Under the electroneutrality approximation, we still account for forces associated with even a small amount of net charge by retaining the body force term in the momentum equation. We refer the reader to Appendix B in the supplementary material for a more detailed derivation of the electroneutrality approximation using perturbation analysis. We express the electroneutrality approximation as

$$\sum_i z_i \left(\frac{\mu_i}{\mu_{i,z_i}} \right) c_i \approx 0. \quad (3.8)$$

In our formulation, we use (3.8) in place of the counter-ion species transport equation (the convective-diffusion equation for c_{CI}) to close the system of governing equations.

This formulation constitutes a total of eight equations for eight unknowns (c_{LE} , c_{TE} , c_{CI} , c_A , u , v , p and ϕ). The final form of the governing equations is

$$\frac{\partial c_i}{\partial t} + \nabla \cdot [\mathbf{u} c_i + z_i \mu_i \mathbf{E} c_i - D_i \nabla c_i] = 0 \quad \text{for } i = \text{LE, TE, A}, \quad (3.9)$$

$$\sum_i z_i \left(\frac{\mu_i}{\mu_{i,z_i}} \right) c_i \approx 0, \quad (3.10)$$

$$\nabla p = \eta \nabla^2 \mathbf{u} + \epsilon [\nabla \cdot \mathbf{E}] \mathbf{E}, \quad (3.11)$$

$$\nabla \cdot \mathbf{u} = 0, \quad (3.12)$$

$$\nabla \cdot \left[E \sum_i z_i \mu_i c_i - \sum_i z_i D_i \left(\frac{\mu_{i,z_i}}{\mu_i} \right) \nabla c_i \right] = 0. \quad (3.13)$$

We performed all numerical simulations with the commercial package COMSOL Multiphysics (version 3.5, COMSOL AB, Stockholm, Sweden) using the Nernst–Planck and incompressible Navier–Stokes modules. We reduced computational cost by axially truncating the channel domain and transforming the flow boundary conditions to a frame of reference moving with the sample zone. The velocity of this frame of reference, U_{zone} , is given in (2.2). The transformed boundary conditions for the species, velocity, pressure and electric potential were the same as those given by Schönfeld *et al.* (2009) and are reproduced in Appendix C of the supplementary material.

We discretized the domain using rectangular mesh elements with a uniform grid density in the radial dimension. We used non-uniform grid spacing in the axial dimension with high resolution in the interface region ($\sim 0.5 \mu\text{m}$) and much lower resolution within the LE and TE zones ($\sim 5 \mu\text{m}$ on average), which remain at steady state. We used a total of 16000 cells throughout the domain. Additionally, we performed tests to assess the grid sensitivity at this resolution and established grid independence. More details regarding domain discretization are provided in Appendix C of the supplementary material.

3.2. Simulation results

We use our numerical simulations to investigate the impact of analyte mobility and non-uniform EOF on sample distributions in ITP. A table with parameter values used in our simulations is provided in Appendix D of the supplementary material. Unless otherwise noted, for this part of our study the simulation parameters reflect the LE and TE chemistry of the validation experiments presented in §5. We non-dimensionalize the applied current density, j , with a characteristic current density j_R . We define j_R as the current density in a non-dispersed ITP process where the LE–TE interface width (δ) is equal to the channel radius (R). The width of the LE–TE interface is given by the one-dimensional theory of MacInnes & Longworth (1932) as

$$\delta \equiv \frac{4R_\mu T}{F U_{ITP}} \frac{\mu_{LE} \mu_{TE}}{\mu_{LE} - \mu_{TE}}. \quad (3.14)$$

The derivation of this result neglects the diffusive component of current density, which is typically small compared to the electromigration component. We therefore express the current density as $j = \sigma_{LE} E_{LE}$, where $\sigma_{LE} = F (z_{LE} \mu_{LE} c_{LE} + z_{CI} \mu_{CI} c_{CI})$ is the LE conductivity. We rearrange (3.14), letting $\delta = R$, to solve for the characteristic current density

$$j_R \equiv \frac{4R_\mu T}{F} \left(\frac{\mu_{TE}}{\mu_{LE} - \mu_{TE}} \right) \frac{\sigma_{LE}}{R}. \quad (3.15)$$

For the simple case of ITP without EOF, an analyte focused at the LE–TE interface has a finite distribution width determined solely by the balance between diffusion and electromigration. Even in this case, the penetration length of the focused analyte into each of its bracketing zones depends strongly on its electrophoretic mobility relative to the LE and TE. For example, an analyte with mobility very near the TE mobility will experience a strong restoring force upon diffusing into the LE zone but a weak restoring force upon diffusing into the TE zone. This results in greater sample penetration into the TE. We demonstrate this effect in figure 2 using area-averaged analyte distributions predicted by simulations of non-dispersed ITP with relatively

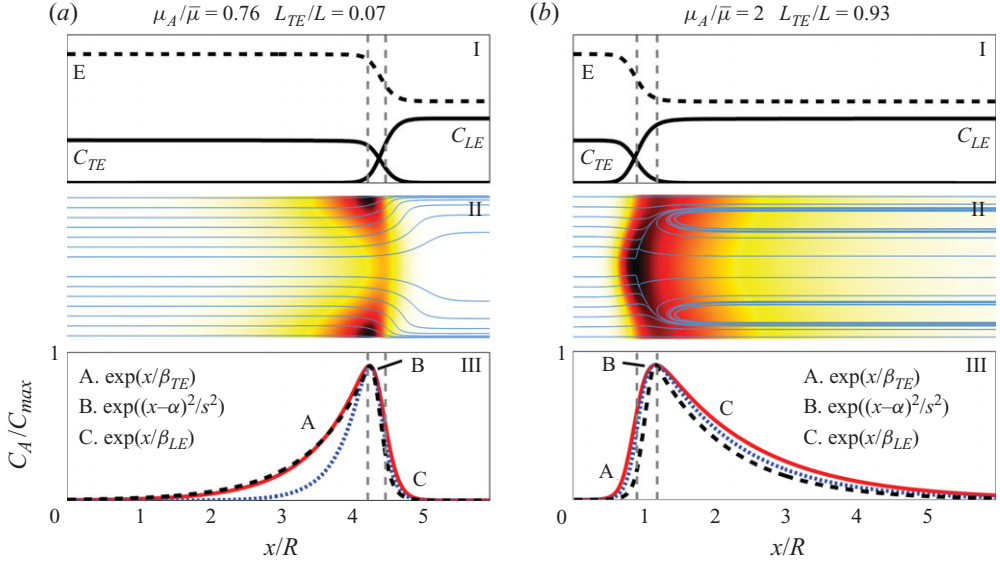


FIGURE 2. Schematic showing the construction of the analytical model and comparing this to area-averaged sample distributions from dispersed and non-dispersed numerical simulations. We fix current density at $j/j_R = 3.13$ and consider two conditions: $\mu_A/\bar{\mu} = 0.76$, $L_{TE}/L = 0.07$ (a) and $\mu_A/\bar{\mu} = 2$, $L_{TE}/L = 0.93$ (b). Here the constant $\bar{\mu}$ (defined in §4.1) is the value of analyte mobility at which the sample distribution is symmetric under non-dispersed conditions ($\mu_{EOF} = 0$). We assume that EO mobility is axially uniform ($\mu_{EOF} = \mu_{EOF}^{TE} = \mu_{EOF}^{LE}$) and consider the case where $\mu_{EOF}/\mu_{LE} = 0.22$ for simulations that include dispersion. Two-dimensional concentration profiles of the dispersed sample are shown in row II along with superimposed lines tangent to combined electromigration and convective mass flux components. The area-averaged distributions corresponding to this dispersed case and to the non-dispersed simulations are shown in row III as red (solid) and blue (dot) curves, respectively. In both cases dispersion affects the already strongly tailing portions of the distributions. The analytical model prediction, which is also shown (dashed curve), is composed of two exponential tails matched to a central Gaussian. The matching points (\tilde{x}_i , defined in §4.1) are shown with vertical dashed lines in row III. These vertical lines extend to row I, where we show the area-average LE and TE species concentrations along with the area-average electric field from simulations including dispersion. The location of the matching points reveals that the tails of the distribution (regions A and C) correspond to the regions of uniform electric field, while the central Gaussian (region B) corresponds to a region of strong electric field gradient.

low- and high-mobility analytes (figures 2a and 2b, respectively). We divide the sample distribution into three parts, corresponding to the two ‘tails’ of the sample distribution (regions A and C) and to its central peak (region B). Under non-dispersed conditions, a low analyte mobility results in strong sample penetration into the TE zone (region A), while a high analyte mobility results in strong penetration into the LE zone (region C).

Figure 2 also shows area-averaged sample distributions from simulations with non-zero EO mobility (solid curves, bottom row). The corresponding area-averaged axial electric field is shown in the top row of figure 2. For figures 2(a) and 2(b), which correspond to relatively low- and high-mobility analytes, respectively, we choose the axial interface position corresponding to a dominant pressure gradient in the zone of greater sample penetration. The resulting strong parabolic flow broadens the distribution tails in these respective zones while leaving the other tail nearly unchanged. We note that the tails of the sample distribution (regions A and

C) occupy regions of approximately uniform electric field while the peak of the distribution (region B) lies within a strong electric field gradient. The regions of uniform electric field correspond to uniform parabolic flow profiles. This suggests that analyte distribution tails primarily experience axially uniform dispersive flow.

The middle row of figure 2 depicts the centreline sample concentration field of the dispersed analytes. Lines tangent to the vector sum of electromigration and advective velocities are also depicted. These images show the interface position-dependent curvature of the sample zone discussed in §2 (see figure 1). In the near-TE-reservoir position (figure 2a) the transverse curvature resembles the favourable parabolic flow in the TE, while in the near-LE-reservoir position (figure 2b) the curvature instead resembles the adverse parabolic flow in the LE. The latter finding regarding pressure gradients is consistent with the numerics of Schönfeld *et al.* (2009), and the analyte peak shape of figure 2(b) is consistent with their qualitative visualizations. In contrast to that work, here we also model the strong effect of analyte mobility relative to the TE and LE, which results in effects of analyte tailing and enhanced dispersion, as described above.

In figure 3 we summarize the dependence of analyte distribution widths (w) on analyte mobility, axial interface position and EO mobility. We use the axial standard deviation of the area-averaged analyte concentration to quantify the distribution width and also as an inverse measure of sensitivity. We plot curves of the analyte distribution width against axial interface position for three analyte mobilities in figure 3(a) and three EO mobilities in figure 3(b). The analyte mobility is compared to a characteristic mobility scale, $\bar{\mu}$, which results in approximately symmetric analyte profiles and is described in detail in §4. Figure 3(a) shows that, in general, dispersion is greatest at the two extremes of the channel, with a minimum width typically achieved within roughly the middle portion of the channel. Analytes with relatively near-TE or near-LE mobility exhibit strong dispersion when near the TE or LE reservoir, respectively. In each case, the most dispersed region corresponds to axial interface positions where the dominant pressure gradient coincides with the zone of greater sample penetration. The intermediate case (where $\mu_A = \bar{\mu}$) has a symmetric distribution with a minimum in dispersion near the channel's axial centre, $L_{TE}/L = 0.5$. By comparison with the other cases where $\mu_A/\bar{\mu}$ is smaller or greater than 1, we note that the point of minimum dispersion is strongly dependent on analyte mobility. In figure 3(b) we consider a fixed analyte mobility ($\mu_A/\bar{\mu} = 0.76$) and vary dimensionless EOF mobility (μ_{EOF}/μ_{LE}) for values commonly observed in glass channels at this pH. For the case of zero dispersion ($\mu_{EOF} = 0$), the analyte distribution width is independent of axial interface position. As EO mobility increases, analyte dispersion increases primarily in the near-TE-reservoir region and remains nearly unchanged elsewhere. Note that for this low-mobility analyte, the width of the distribution is approximately insensitive to the magnitude of the pressure gradient in the LE, as all of the curves shown in figure 3(b) approach the same value in the $L_{TE}/L > 0.5$ region. Additionally, both of the dispersed curves shown in figure 3(b) (and others we examined) have a point of minimum dispersion around $L_{TE}/L = 0.8$. This suggests that the point of minimum dispersion is at most weakly dependent on EO mobility.

To aid in later comparisons with experimental data, we approximated the diffractive effects of microscope imaging on simulation data. In figures 6 and 7, which are discussed at length in §5, we convolve our numerical data with a three-dimensional optical point spread function (PSF) that accounts for diffraction introduced by the microscope objective. In this three-dimensional convolution, we account for the varying values of magnification at each plane relative to the focal plane. Under the

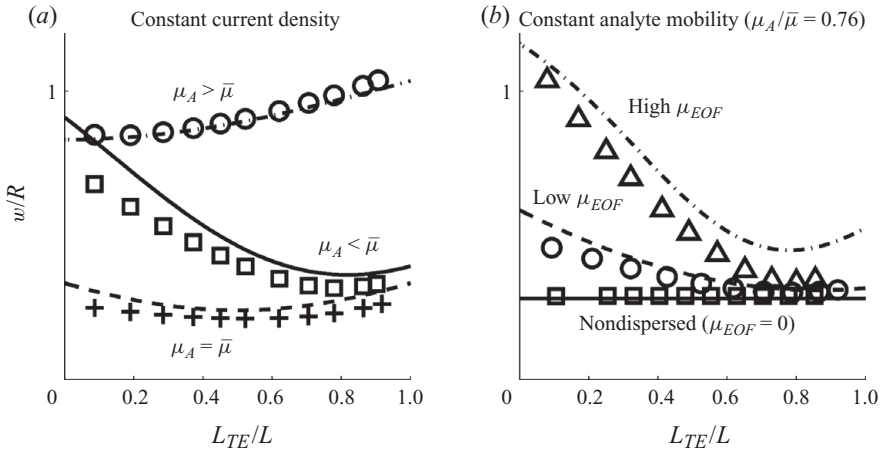


FIGURE 3. Comparison of area-averaged simulation results (data symbols) and analytical model predictions (curves) for the sample zone width as a function of axial interface position. We alternately hold EO mobility constant and vary the analyte mobility (a) or hold the analyte mobility constant and vary EO mobility (b). In all cases the current density, j/j_R , is 4.17. We use the standard deviation to quantify the sample distribution width, w . (a) We hold the EO mobility constant ($\mu_{EOF}/\mu_{LE} = 0.22$) and show realizations for $\mu_A/\bar{\mu} = 0.76, 1$ and 2 . The $\mu_A < \bar{\mu}$ case is most dispersed for $L_{TE}/L < 0.5$, where the TE pressure gradient is dominant. Conversely, an analyte with $\mu_A > \bar{\mu}$ is most dispersed when LE pressure gradients are dominant ($L_{TE}/L > 0.5$). A symmetric sample zone ($\mu_A = \bar{\mu}$) is affected to a lesser degree by dispersion and so reaches its minimum width near $L_{TE}/L = 0.5$. The analytical model captures these trends very well. (b) We hold analyte mobility constant at $\mu_A/\bar{\mu} = 0.76$ and consider three values of the EO mobility, $\mu_{EOF}/\mu_{LE} = 0, 0.07$ and 0.29 . The simulation and analytical model show very good agreement in all cases. The width of the non-dispersed ($\mu_{EOF} = 0$) sample distribution is independent of axial interface position, whereas both dispersed cases show strong dispersive broadening particularly for $L_{TE}/L < 0.5$. In this region we expect Taylor–Aris-type dispersion in the TE zone to dominate the distribution width of relatively low mobility analytes. Note also that the point of minimum dispersion predicted by the simulations and analytical model is $L_{TE}/L \approx 0.8$ in both cases, and therefore seems to be independent of EO mobility.

optical conditions of the validation experiments (see § 5), roughly $3 \mu\text{m}$ of the channel's depth (near the centreline) is contained within the depth of field. We summarize the process of generating and applying the PSF in Appendix E of the supplementary material and will discuss it in more detail in a future publication.

4. Area-averaged analytical model for sample dispersion

4.1. Theory

We present an analytical model for the area-averaged concentration distribution of analytes focused by ITP in the presence of non-zero EO slip. The model leverages Taylor–Aris-type dispersion analysis to produce a closed-form description of the analyte width across a wide range of ITP conditions (Taylor 1953; Aris 1956). We partition the focused analyte distribution into three regions: the LE–TE interface itself, the section tailing into the TE zone and the section tailing into the LE zone. These regions are depicted, respectively, as regions B, A and C in figure 2. The shapes of regions A and C are strong functions of the value of the analyte mobility (μ_A) relative to the TE and LE mobilities as well as the local pressure gradients within the TE and LE zones.

The unsteady time scale is the time for the ITP zone to move a significant fraction of the channel length, $L/|U_{zone}|$. This value is on the order of 100 s for the regimes of interest here and is thus significantly larger than the time scales associated with diffusion and electromigration, both on the order of 0.1 s (see below for a discussion of relevant dispersion time scales). We therefore assume quasi-steady-state dispersion throughout the channel length. We approximate focusing dynamics in A and C by assuming that these regions have a uniform axial pressure gradient and electric field. In region B, we approximate the electric field as a linear function of the axial dimension, x . In constructing this approximate model, we assume that all variables are uniform in the radial dimension, r . For each of the three regions, the steady-state flux conservation equation for the area-averaged analyte concentration (Bharadwaj *et al.* 2008) in a frame of reference moving with the ITP zones (U_{zone} , see (2.2)) is

$$\frac{d}{dx} \left[\left(\mu_A E c_A + \bar{U}_{EOF} c_A - D_{eff} \frac{dc_A}{dx} \right) - U_{zone} c_A \right] = 0. \quad (4.1)$$

Here E is the axial electric field, c_A is the (area-averaged) analyte concentration, \bar{U}_{EOF} is the axial-average EOF velocity and D_{eff} is the analyte effective Taylor dispersion diffusivity (Taylor 1953; Aris 1956; Bharadwaj *et al.* 2008). We can generally separate and integrate (4.1) for the analyte concentration assuming zero concentration sufficiently far from the LE–TE interface to find

$$c_A = K_i \exp \left(\int \frac{\mu_A E - U_{ITP}}{D_{eff}} dx \right), \quad (4.2)$$

where K_i is a constant of integration. As mentioned above, we approximate the electric field as uniform sufficiently far from the LE–TE interface and linear across this boundary. In regions A and C, the effective diffusivity is determined by the pressure gradient in the TE and LE, respectively:

$$D_{eff,i} = D_A \left[1 + \frac{1}{48} \left(\frac{R\bar{U}_i}{D_A} \right)^2 \right], \quad (4.3)$$

where

$$\bar{U}_i \equiv \mu_{EOF}^i E_i - \left[\left(\frac{L_{TE}}{L} \right) \mu_{EOF}^{TE} E_{TE} + \left(1 - \frac{L_{TE}}{L} \right) \mu_{EOF}^{LE} E_{LE} \right]. \quad (4.4)$$

The subscript i denotes the TE or LE regions (respectively A and C in figure 2). \bar{U}_i is the magnitude of the dispersive (parabolic) flow component, whose area average is equal to the difference between the local and axial-average EO velocities.

We can therefore express (4.2) separately for regions A, B and C as follows:

$$c_A^{TE} = K_{TE} \exp \left[\left(\frac{\mu_A E_{TE} - U_{ITP}}{D_{eff,TE}} \right) x \right], \quad (4.5a)$$

$$c_A^{INT} = K_{INT} \exp \left[\frac{1}{D_A} \int \left(\mu_A \left(\frac{\Delta E}{a\delta} x + \bar{E} \right) - U_{ITP} \right) dx \right], \quad (4.5b)$$

$$c_A^{LE} = K_{LE} \exp \left[\left(\frac{\mu_A E_{LE} - U_{ITP}}{D_{eff,LE}} \right) x \right]. \quad (4.5c)$$

Here c_A^{TE} , c_A^{INT} and c_A^{LE} are the analyte concentrations in the TE, interface and LE regions, respectively. K_{TE} , K_{INT} and K_{LE} are the corresponding constants of integration. \bar{E} is the arithmetic average of the (axial) electric fields,

$\bar{E} \equiv (E_{TE} + E_{LE})/2$, and the difference in the electric field between the LE and TE zones is denoted as $\Delta E \equiv E_{LE} - E_{TE}$. We hypothesize that the contribution of the interface region (region B) to the distribution width is negligible when compared to its dispersed tails (regions A and C). We further assume that the interface region is well-modelled without accounting for dispersion. In (4.5b), we therefore use the analyte diffusivity, D_A , in place of D_{eff} . We also write the electric field in this region in terms of the diffusion-limited width of the interface, $a\delta$. The dimensionless constant a is the prefactor introduced to scale the LE–TE interface width as given by the simple relation in (3.14). In our model, this prefactor determines the slope of the electric field at the LE–TE interface, neglecting dispersion. We determined the value of a by analysing the electric field gradient of area-averaged numerical simulations of ITP neglecting dispersion, similar to those performed by Khurana & Santiago (2008). For a fairly wide range of applied current densities, we find that a prefactor value of $a \approx 1.58$ best describes the slope of the electric field at its point of inflection (located within region B). We refer the reader to Appendix F for further details on the determination of a .

Lastly, we determine analytically the coefficients K_i of each region by imposing three matching conditions to produce a composite, smooth, area-averaged concentration distribution: (i) function values must be equal at both matching points, \tilde{x}_i (i.e. the A–B and B–C interfaces), (ii) function derivatives must be equal at both matching points (to guarantee smoothness of the distribution) and (iii) the integral of the composite solution must reflect the total amount of accumulated sample. We note that continuity of the electric field is not ensured under these conditions.

By imposing these conditions and solving (4.5a)–(4.5c) we arrive at the following composite solution for the one-dimensional (area-averaged) sample distribution along the axial dimension, x :

$$c_A(x) = K \begin{cases} \exp\left[\frac{\alpha}{\beta_{TE}} + \frac{s^2}{(2\beta_{TE})^2}\right] \exp\left[\frac{x}{\beta_{TE}}\right], & x < \tilde{x}_{TE} \\ \exp\left[-\frac{(x + \alpha)^2}{s^2}\right], & \tilde{x}_{TE} < x < \tilde{x}_{LE}, \\ \exp\left[\frac{\alpha}{\beta_{LE}} + \frac{s^2}{(2\beta_{LE})^2}\right] \exp\left[\frac{x}{\beta_{LE}}\right], & x > \tilde{x}_{LE} \end{cases} \quad (4.6)$$

where

$$\tilde{x}_i = \frac{s^2}{2\beta_i} - \alpha, \quad (4.7)$$

$$\frac{\beta_{LE}}{\delta} = \frac{1}{4} \frac{\mu_A(\mu_{LE} - \mu_{TE})}{\mu_{TE}(\mu_A - \mu_{LE})} \frac{D_{eff,LE}}{D_A}, \quad (4.8)$$

$$\frac{\beta_{TE}}{\delta} = \frac{1}{4} \frac{\mu_A(\mu_{LE} - \mu_{TE})}{\mu_{LE}(\mu_A - \mu_{TE})} \frac{D_{eff,TE}}{D_A}, \quad (4.9)$$

$$\frac{s}{\delta} = \sqrt{\frac{a}{2}}, \quad (4.10)$$

$$\frac{\alpha}{\delta} = a \left[\frac{1}{2} - \frac{\mu_{LE}}{\mu_A} \left(\frac{\mu_A - \mu_{TE}}{\mu_{LE} - \mu_{TE}} \right) \right]. \quad (4.11)$$

Here β_i and s naturally arise as characteristic length scales for the regions of uniform and linear electric field, respectively. α is an axial displacement (relative to the centre of the LE–TE interface) of the peak value of the central Gaussian portion of the curve (see region B in figure 2). The constant K normalizes the distribution so that its axial integral reflects the total accumulated amount of sample. We note that the matching points, \tilde{x}_i , are entirely determined by the continuity and smoothness conditions above.

An important contribution of this model is that it accounts for analyte properties (e.g. analyte mobility) in determining the distribution width. To establish a basis of comparison between relatively low and relatively high values of analyte mobility, we can derive the analyte mobility that results in an approximately symmetric distribution, $\bar{\mu}$. A symmetric distribution results when the analyte focuses in the central portion of the electric field gradient ($x=0$ in figure 2) such that the tails in regions A and C decay over the same length scale (i.e. when $\beta_{TE} = -\beta_{LE}$). In our analytical model, the location of the analyte peak is governed by the parameter α , which shifts the position of the central Gaussian of region B. These conditions are satisfied by letting $\alpha = 0$ (or, equivalently, by letting $\beta_{TE} = -\beta_{LE}$ and $D_{eff,i} = D_A$) and solving for the resulting analyte mobility. Thus, the analyte mobility resulting in a symmetric distribution is

$$\bar{\mu} = \frac{\mu_{LE}\mu_{TE}}{\frac{1}{2}(\mu_{LE} + \mu_{TE})}. \quad (4.12)$$

For $\mu_A < \bar{\mu}$ we expect that the sample will have a longer penetration length in the TE, while for $\mu_A > \bar{\mu}$ we expect a longer penetration length in the LE.

In addition to $\mu_A/\bar{\mu}$, we also use $(\mu_A - \mu_{TE})/(\mu_{LE} - \mu_{TE})$ as a non-dimensional parameter describing analyte mobility. The latter parameter appears in (4.11) and varies from a minimum value of zero (where $\mu_A = \mu_{TE}$) to a maximum value of 1 (where $\mu_A = \mu_{LE}$). Analytes with effective mobility outside this range do not focus. We use this normalization parameter for the contour maps in figure 4 and elsewhere use $\bar{\mu}$ as a non-dimensional parameter describing analyte tailing.

Before continuing, we note that the main assumption underlying Taylor–Aris dispersion analysis is that the time scale of radial diffusion, t_r , should be small compared to the time scale(s) of axial dispersion, t_{disp} . The radial diffusion time is $t_r = R^2/D_A$ and, under typical conditions, has a value on the order of 0.1 s. There are several possible time scales for the dispersion process. These include the unsteady time scale, $L/|U_{zone}|$ (discussed above), and the characteristic focusing time associated with analyte axial electromigration, $\lambda/|U_A|$ (here $U_A = \mu_A E_i - U_{ITP}$ is the relative velocity of the analyte with respect to the moving LE–TE interface and λ is the length of the analyte zone). However, these time scales do not account for the direct dependence of the dispersive process on EO mobility. Thus, perhaps the most relevant is an axial dispersion time scale governed by the magnitude of the non-uniform flow component of the velocity and the characteristic length scale of the analyte zone, $t_{disp} = \lambda/|\mu_{EOF}\Delta E|$. Here, we find the velocity magnitude by evaluating (4.4) for the highest value of \bar{U}_i (cf., figure 1). The length of the analyte zone, λ , scales as the tailing dimension β_i . For a symmetric analyte, $\mu_A \approx \bar{\mu}$, tailing is minimal and t_{disp} is on the order of 0.1 s. For cases with significant tailing (e.g. $\mu_A < \bar{\mu}$), λ increases and the value of t_{disp} can be on the order of 1 s. While the condition $t_r \ll t_{disp}$ does not always hold strictly, we believe that the Taylor–Aris analysis is a useful approximation for modelling dispersion in ITP under a wide variety of conditions. As we will show, the Taylor–Aris approximation leads to very good agreement between our area-averaged model, numerical simulations and experiments.

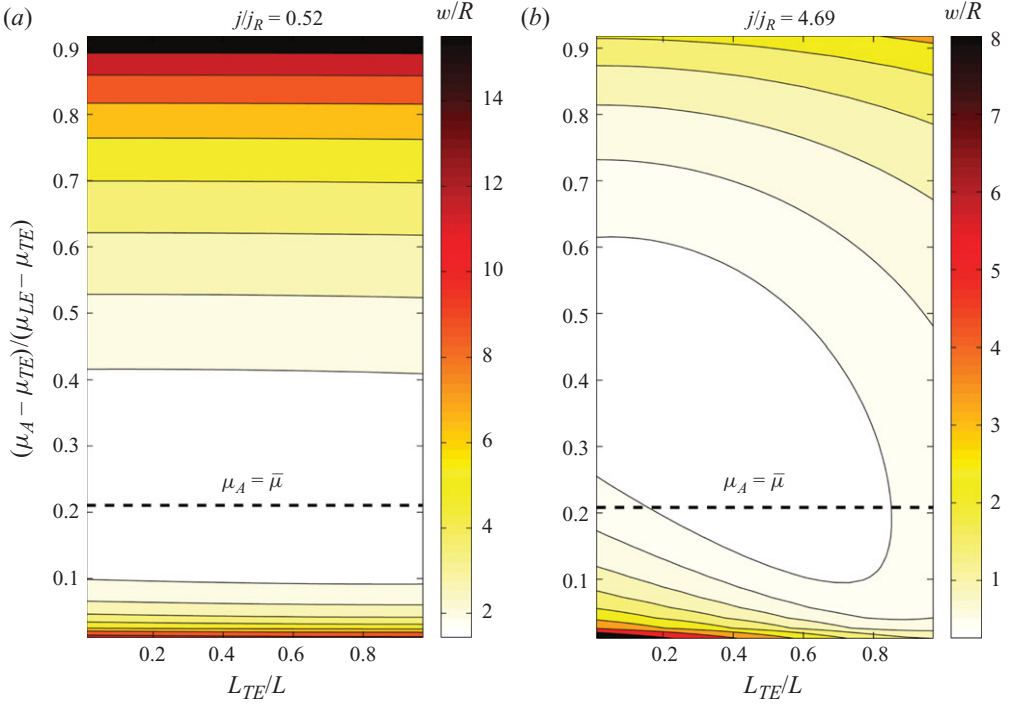


FIGURE 4. (Colour online available at journals.cambridge.org/FLM) Contours of the (base 10) logarithm of the normalized axial analyte distribution width (w/R) predicted by our analytical model for varying dimensionless axial position and normalized analyte mobility. We assume an axially uniform normalized EO mobility, μ_{EOF}/μ_{LE} , of 0.22. The non-dimensional parameter $(\mu_A - \mu_{TE})/(\mu_{LE} - \mu_{TE})$ describes the analyte mobility relative to that of the TE and LE. Analytes outside the range of $(\mu_A - \mu_{TE})/(\mu_{LE} - \mu_{TE}) = 0$ to 1 do not focus. (a) At a low applied current density ($j/j_R = 0.52$), dispersion is diffusion-limited, so the sample distribution width varies only with the normalized analyte mobility about a minimum of $(\mu_A - \mu_{TE})/(\mu_{LE} - \mu_{TE}) \approx 0.21$, which corresponds to the symmetric analyte mobility, $\mu_A = \bar{\mu}$. (b) At a high applied current density ($j/j_R = 4.69$), the distribution also depends on the interface position. Here, analyte widths increase for either analytes tailing towards a TE with strong dispersive velocity (lower-left corner) or analytes tailing towards a LE with strong dispersive velocity (upper-right corner).

4.2. Results of the analytical model and comparison with numerical simulations

Our model shows good agreement with the area-averaged distributions taken from numerical simulations for a variety of analyte mobilities, as shown in the bottom row of figure 2. In each case, the model captures the significant differences in length scales between the LE and TE tails, as predicted by the numerical simulations. This agreement supports our analytical model's estimate of the length scale parameters, β_i , associated with distribution tails. The vertical dashed lines in the top and bottom rows of figure 2 represent the matching points for the analytical model. As constructed, these matching points delineate regions of approximately uniform electric field from the high electric field gradient of the LE–TE interface. We note that the central Gaussian of the predicted distribution shifts location within region B (the region of linear electric field) depending on analyte mobility. The analyte peak shifts nearer the TE in figure 2(a), where $\mu_A < \bar{\mu}$, and nearer the LE in figure 2(b), where $\mu_A > \bar{\mu}$. Figure 3 presents a more quantitative comparison of simulation widths predicted by

the analytical model and numerical simulations. Here analytical model predictions of the sample distribution width show excellent agreement with simulations over a wide range of conditions varying analyte mobility, applied current density and axial position of the interface.

Having corroborated our analytical model with numerical simulations (cf., figures 2 and 3), we now use this model to explore the dependence of the distribution width on a continuum of values of analyte mobility and axial interface position. Figure 4 shows contour maps of the analyte distribution width (scaled by the channel radius, R) as it varies with axial interface position and analyte mobility. Figures 4(a) and 4(b) respectively explore the cases of relatively low and high applied current densities, $j/j_R = 0.52$ and 4.69 respectively. These values correspond to applied current densities of 0.80 and 7.16 A cm^{-2} . For the lower applied current density, dispersion is diffusion-limited (dominated by the balance of diffusion and electrophoretic restoring fluxes) and therefore varies only with analyte mobility. Note that analyte mobility relative to that of the TE and LE plays a key role in determining the sample zone width. For example, dispersion is negligible in figure 4(a) and yet w/R can vary significantly with the non-dimensional mobility parameter. The distribution width is minimum for $\mu_A = \bar{\mu}$, as per our derivation of (4.12), and significantly greater when μ_A approaches either the mobility of the LE or TE. For example, for values of the scaled mobility parameter of 0.2 and 0.9 , w/R equals approximately 2 and 15 , respectively. At higher current densities, the effect of analyte mobility is compounded by the growing importance of advective dispersion. Collectively, this results in a slanting of the w/R contours. Dispersion is greatest in two regions, namely the bottom-left and top-right corners of the plot. These regions correspond, respectively, to sample penetration in the TE with dominant TE pressure gradient and sample penetration in the LE with dominant LE pressure gradient.

Figure 5 shows contour maps of the analyte distribution width as it varies with axial interface position and EO mobility for $\mu_A/\bar{\mu} = 1, 1.2$ and 2 . Depending on the value of the EO mobility, the interface can have positive or negative velocity. These two cases correspond to initial conditions discussed in §2, where the channel is entirely filled with LE or TE, respectively. The dashed lines are drawn where the interface has zero velocity (i.e. where the bulk EOF velocity balances electromigration, $U_{EOF} = -U_{ITP}$). For $\mu_A/\bar{\mu} = 1$, the width of the distribution is symmetric about $L_{TE}/L = 0.5$. For increasing analyte mobility, the location of the minimum analyte zone width moves towards the LE reservoir (figure 5b). Above about $\mu_A/\bar{\mu} = 1.9$ (see figure 5c), the local analyte zone width always increases with increasing L_{TE}/L .

We validate our model and simulations by comparison with experiments in figures 6 and 7. Correspondingly, the predictions in these figures explore analytes with approximately symmetric and with near-TE mobilities. As with the numerical simulations, we account for optical convolution effects for a better comparison with experiments. To this end, we apply a one-dimensional convolution with a Gaussian kernel whose width is determined by comparison of the simulation area-averaged distribution with and without the three-dimensional convolution. These data are discussed at greater length in the next section.

5. Experimental validation

5.1. Materials, buffer chemistry and experimental apparatus

We performed single-interface peak mode ITP experiments to validate our numerical and analytical models. We used 100 mM HCl for the LE, 100 mM

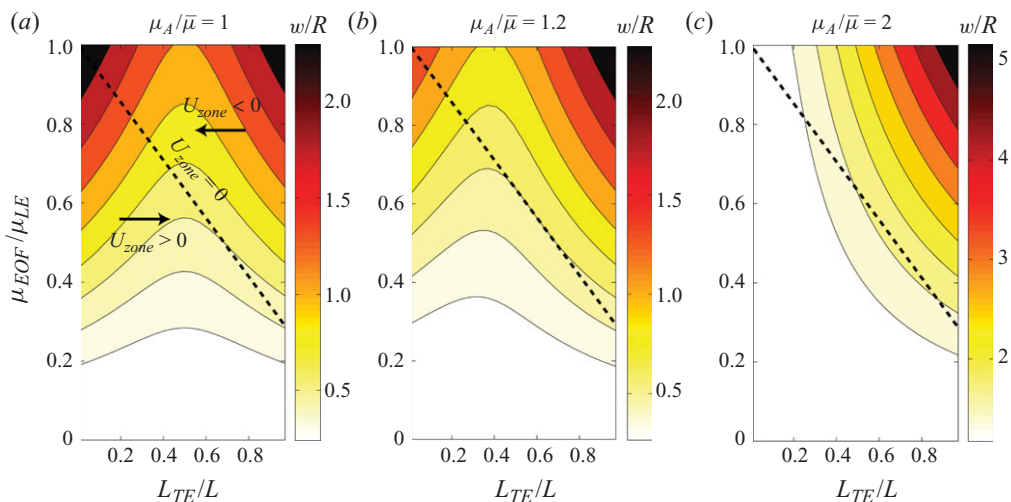


FIGURE 5. (Colour online) Contours of the (base 10) logarithm of the normalized axial analyte distribution width, w/R , predicted by our analytical model for varying dimensionless axial position, L_{TE}/L , and normalized EO mobility, μ_{EOF}/μ_{LE} . We hold current density constant ($j/j_R = 3.13$) and, for simplicity, assume $\mu_{EOF} = \mu_{EOF}^{TE} = \mu_{EOF}^{LE}$. We show separate contour maps for normalized analyte mobility values of $\mu_A/\bar{\mu} = 1, 1.2$ and 2 . The dashed line is drawn where the interface tends to zero velocity (i.e. where bulk EOF balances electromigration, $U_{EOF} = -U_{ITP}$). Solutions to the left of this line are for positive interface velocities, for experiments where the channel is initially filled with LE. To the right, we show solutions for which interface velocity is negative, so that the channel is initially filled with TE and the zone travels into the channel in the direction of EOF. For the latter case, $\mu_{EOF}^{TE} E_{TE} > U_{ITP}$ is a necessary condition for the interface to enter the channel from the LE reservoir. (a) For a symmetric sample distribution ($\mu_A/\bar{\mu} = 1$), the contour map is symmetric about $L_{TE}/L = 0.5$ and the distribution width may reach a minimum at this point of symmetry. (b)–(c) As the analyte mobility increases, the location of this minimum shifts towards lower values of L_{TE}/L (e.g. near $L_{TE}/L = 0.3$ when $\mu_A/\bar{\mu} = 1.2$) and vanishes altogether for $\mu_A/\bar{\mu}$ of about 1.9 or greater.

2-(*N*-morpholino)ethanesulphonic acid (MES) for the TE and 200 mM Bis-Tris as the background buffering ion. We added 2 mM Ba(OH)₂ to the TE in order to minimize zone broadening due to focusing of carbonic acid (see Khurana & Santiago 2009). We also prepared 1 μ m stock solution of Alexa Fluor 488 (Invitrogen, Carlsbad, CA) and fluorescein (J.T. Baker, Phillipsburg, NJ), which we used to visualize a sample zone focused in peak mode (anionic) ITP. All solutions were prepared in UltraPure DNase/RNase free distilled water (GIBCO Invitrogen, Carlsbad, CA). The chemical properties for HCl, MES and Bis-Tris were obtained from the PeakMaster 5.1 database (Jaroš *et al.* 2004), which contains fully ionized mobility and pKa values determined by Hirokawa *et al.* (1983). We determined the fully ionized mobility of Alexa Fluor 488 ($-37 \times 10^{-9} \text{ m}^2 \text{ V}^{-1} \text{ s}^{-1}$) through on-chip capillary electrophoresis. For fluorescein, we chose the effective mobility to result in the best fit with simulation and model predictions. The resulting value ($-18.9 \times 10^{-9} \text{ m}^2 \text{ V}^{-1} \text{ s}^{-1}$) is within the uncertainty bounds of values reported in the literature (Martin & Lindqvist 1975; Mchedlov-Petrosyan, Kukhtik & Alekseeva 1994; Shakalisava *et al.* 2009) and accepted models for ionic strength correction (Bahga, Bercovici & Santiago 2010).

We obtained images using an inverted epifluorescent microscope (IX70, Olympus, Hauppauge, NY) equipped with an LED lamp (LEDC1, Thor Labs, Newton, NJ) and U-MWIBA filter-cube from Olympus (460–490 nm excitation, 515 nm emission and

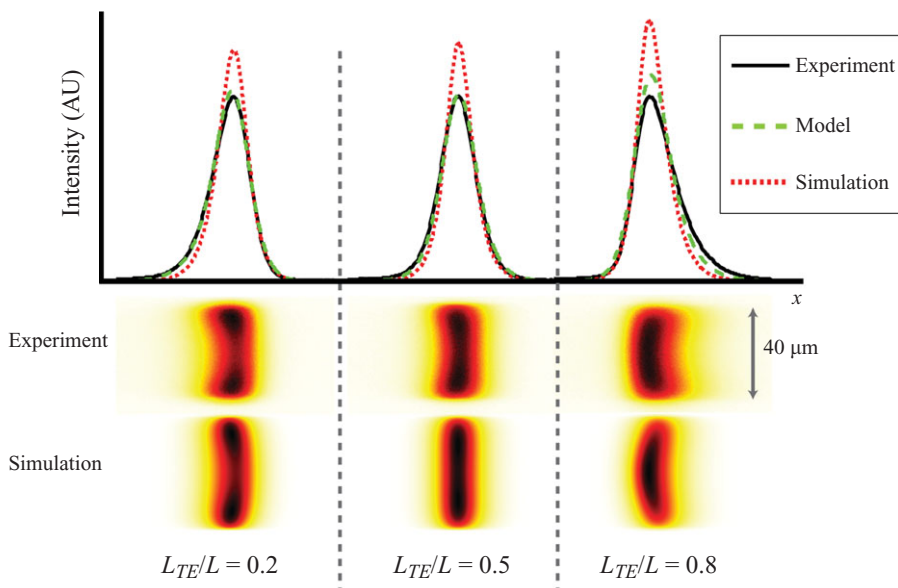


FIGURE 6. Comparison of our numerical simulations and analytical model with experiments of focused Alexa Fluor 488 for $j/j_R = 3.13$. We normalize all distributions to represent equal amounts of focused sample (i.e. all curve or area integrals normalized to unity). Simulation distributions are adjusted to account for optical diffraction effects through convolution of the simulation data with the theoretical three-dimensional PSF corresponding to the microscope objective. The analytical model inherently reflects a cross-sectional-area average, and so axial distributions are adjusted by approximating the optical three-dimensional convolution as a one-dimensional convolution with a Gaussian. The simulations and model are in very good agreement with experiments in both the two-dimensional and area-averaged distributions. The conditions shown here are representative of both a typical ITP buffer chemistry and value of applied current density. For these experiments we used a $20\times$ objective with 0.5 numerical aperture, 10 ms exposure time and a $40\mu\text{m}$ inner diameter fused silica capillary.

505 nm cutoff dichroic). We used a $20\times$ (NA = 0.5, WD = 2.1 mm) UPlanFl objective for Alexa Fluor 488 experiments and a $10\times$ (NA = 0.4, WD = 3.1 mm) UPlanApo objective for fluorescein experiments, both also from Olympus. We captured images using a 12 bit, 1300×1030 pixel array CCD camera (Coolsnap-fx 16s, Princeton Instruments, Trenton, NJ). We controlled the camera using Winview32 (Princeton Instruments, Trenton, NJ) and processed the images with MATLAB (R2007b, Mathworks, Natick, MA). We triggered the camera at 10 Hz (Alexa Fluor 488 experiments) and 5 Hz (fluorescein experiments) with an external signal generator (model 33220A, Agilent Technologies, Santa Clara, CA). We chose relatively low exposure times of 10 ms (Alexa Fluor 488 experiments) and 20 ms (fluorescein experiments) to avoid smearing due to motion of the sample plug.

We performed all experiments in $40\mu\text{m}$ inner diameter circular fused silica capillaries (TSP040375, Polymicro Technologies, Phoenix, AZ). We removed the capillary protective (and fluorescent) polyimide coating with the flame of a lighter to expose the fused silica. We immobilized the capillaries on a microscope slide with instant adhesive (401, LOCTITE, Rocky Hill, CT). We fabricated reservoirs using threaded 1.5 ml tubes (64115, E&K Scientific, Santa Clara, CA) and used UV-curing optical adhesive (no. 63, Norland Optical, Cranbury, NJ) to bond them to the surface at each end of the capillary. We covered the length of the capillary with a layer of

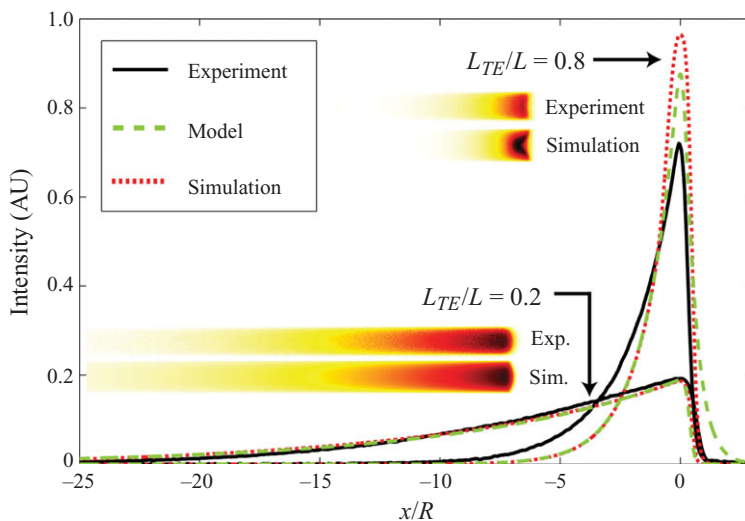


FIGURE 7. (Colour online) Experimental data showing the combined effects of analyte mobility, dispersion due to EOF and axial interface position on the sample distribution in a single experiment. Shown together with the experiments are predictions from the analytical model and simulations for $j/j_R = 6.26$. The visualized analyte is fluorescein, and the LE and TE buffers are the same as in figure 6. The analyte's mobility is near the TE mobility ($\mu_A < \bar{\mu}$), which causes it to focus off-centre (towards the TE) with respect to the LE–TE interface. The strong pressure gradient in the TE zone at $L_{TE}/L = 0.2$ results in strong dispersive broadening of the left sample tail into the TE. At $L_{TE}/L = 0.8$, the TE pressure gradient is much weaker, resulting in a $3 \times$ increase in peak signal intensity over the previous case. The inset images show experiments and optical-function-corrected sample distribution images from simulations. For these experiments we used a $10 \times$ objective with 0.4 numerical aperture, 20 ms exposure time and a $40 \mu\text{m}$ inner diameter fused silica capillary.

the same (index-matching) adhesive in order to minimize the optical distortion due to curvature at the glass–air boundary. We carried out all experiments at constant applied currents of $6 \mu\text{A}$ ($j/j_R = 3.13$) or $12 \mu\text{A}$ ($j/j_R = 6.26$) using a sourcemeter (model 2410, Keithley Instruments, Cleveland, OH).

We determined the LE and TE EO mobilities (μ_{EOF}^{TE} , μ_{EOF}^{LE}) individually for each experiment. To do this, we calculated the velocity of the sample zone at several axial positions in the channel using a custom image processing code. We then determined the expected values of μ_{EOF}^{TE} and μ_{EOF}^{LE} using a least-squares optimization on (2.2).

5.2. Experimental results

We validate the numerical simulations and analytical model presented in the previous sections with controlled and repeatable experimental observations. We performed focusing experiments using Alexa Fluor 488 (AF488) as an analyte. Under these conditions, AF488 has an electrophoretic mobility approximately equal to the mobility resulting in a symmetric sample distribution ($\mu_A \approx \bar{\mu}$). Figure 6 shows results for the analytical model and simulation and compares these with experimental visualizations of focused AF488. As discussed in §§3 and 4, optical effects introduced by the microscope objective are accounted for in the numerical simulations and analytical model. The qualitative agreement between experimental visualizations and simulation images is very good. Note that the simulations correctly predict the changing curvature of the plug as well as the near-wall sample accumulation for near-TE-reservoir interface locations. The simulations predict a slightly higher peak value for the

area-averaged distribution than that observed in experiments but nonetheless capture the axial dependence of distribution tailing. Sample distributions predicted by the analytical model show excellent agreement with experiments.

In figure 7 we consider the more dramatic case of fluorescein as the focused sample. Under these conditions, the value of the parameter $\mu_A/\bar{\mu}$ is approximately 0.66, predicting strong tailing towards the TE. Shown are experimental data together with predictions from both simulation and our analytical model. The TE and LE buffers are identical to those of figure 6 in order to highlight the dramatic effect of analyte mobility on distribution shape. The strong skew and tailing of the fluorescein distribution makes the peak width sensitive to the pressure gradients in the TE zone. At $L_{TE}/L=0.2$, the measured standard deviation width is approximately six times greater than the diffusion-limited (non-dispersed) minimum width due to strong analyte tailing into the locally dispersive TE zone. For a near-LE-reservoir position of $L_{TE}/L=0.8$, the TE pressure gradient is much weaker and dispersive broadening decreases significantly. For the latter case, the maximum analyte concentration increases by roughly a factor of 3 over the case where $L_{TE}/L=0.2$. The comparison of fluorescein distribution between $L_{TE}/L=0.2$ and 0.8 shows the dramatic effect of analyte position on dispersion. This particular case of analyte dispersion due to the combined effects of analyte mobility and EOF-associated dispersion shows that detector placement can be of great importance in ITP assays with non-negligible EOF. Once again, our model and simulations show good agreement with experimental data. The only significant difference is in the $L_{TE}/L=0.2$ case, where the simulation and model predict a significantly higher maximum concentration than found in experiments. Nevertheless, the simulation and model capture the significant trends including the shape of the sample distribution and the sharp increase in peak concentration due to decreased dispersion in the TE. Once again, as in figure 6, the concentration distributions predicted by the analytical model show very good agreement with experiments.

6. Summary and conclusions

Analytes focused in peak mode ITP show strong penetration into the TE if their mobility is near that of the TE and strong penetration into the LE if their mobility is near that of the LE. This penetration can cause strongly asymmetric ‘tails’ in the distribution, even in the absence of advective dispersion. Advective dispersion can be generated by axially non-uniform EOF and leads to further peak-broadening. Gradients in electric field are established by axial conductivity gradients and can couple with non-zero zeta potentials to lead to the generation of internal pressure gradients and secondary flows. These internal pressure gradients are approximately uniform within the LE and TE zones (away from the ITP interface), and their relative magnitudes are determined by the axial position of the ITP interface along the channel. Strong TE pressure gradients arise when the interface is near the TE reservoir, and strong LE pressure gradients arise when the interface is near the LE reservoir. The dispersive velocities associated with these local pressure gradients broaden analyte distributions that tail into the TE or LE, respectively.

We have developed and experimentally validated numerical and analytical models of sample zone dispersion due to analyte mobility effects and non-uniform EOF in peak mode ITP. Our numerical simulations show that analyte properties coupled with local pressure gradients in the LE and TE play a key role in dispersion of focused species. We constructed our analytical model based on this finding. In addition

to taking analyte properties into account, this model incorporates effects of local pressure gradients through separate Taylor–Aris-type dispersion coefficients for the LE and TE regions. We validated our model and simulations with well-controlled visualizations of two different fluorescent analytes focused in peak mode ITP. An important conclusion of our study is that the analyte zone width in peak mode ITP is mostly controlled by dispersion in regions immediately adjacent but not within the analyte peak itself. The overall analyte zone width is therefore mostly governed by dispersion processes in regions of locally uniform electric field and secondary fluid flow. This is fortunate, as the peak region itself can contain strong radial gradients of velocity, electric potential and species concentration which are difficult to model. We found that even a simple treatment of this complex central peak region (here we simply use axial molecular diffusion) is sufficient in capturing the overall analyte width, provided the adjacent regions are well modelled by considering a coupling of dispersion dynamics and focusing due to analyte electromigration.

Our area-averaged model provides fast and accurate predictions of sample zone concentration distribution based on known parameters such as species electrophoretic mobilities, EO mobility, current density and channel dimensions. To our knowledge, this is the first analytical model of dispersion in ITP to take into account analyte properties. This is also the first time that the coupling of analyte tailing and local pressure gradients has been identified as the dominant mechanism for sample dispersion in peak mode ITP.

We gratefully acknowledge funding from DARPA sponsored Micro/Nano Fluidics Fundamentals Focus (MF3) Center under contract number N66001-10-1-4003, and from DARPA grant N660001-09-C-2082. G.G.-S. is supported by a Stanford School of Engineering graduate fellowship. M.B. is supported by an Office of Technology Licensing Stanford Graduate Fellowship and a Fulbright Fellowship. The authors thank Denitsa Milanova for sharing her experimental measurements of fluorophore mobility.

Supplementary material is available at journals.cambridge.org/flm.

REFERENCES

- ALBERTY, R. A. 1950 Moving boundary systems formed by weak electrolytes. Theory of simple systems formed by weak acids and bases. *J. Am. Chem. Soc.* **72** (6), 2361–2367.
- ANDERSON, J. L. & IDOL, W. K. 1985 Electroosmosis through pores with nonuniformly charged walls. *Chem. Engng Commun.* **38** (3), 93.
- ARIS, R. 1956 On the dispersion of a solute in a fluid flowing through a tube. *Proc. R. Soc. Lond. A* **235** (1200), 67–77.
- BAHGA, S. S., BERCOVICI, M. & SANTIAGO, J. G. 2010 Ionic strength effects on electrophoretic focusing and separations. *Electrophoresis* **31** (5), 910–919.
- BHARADWAJ, R., HUBER, D. E., KHURANA, T. & SANTIAGO, J. G. 2008 Taylor dispersion in sample preconcentration methods. In *Handbook of Capillary and Microchip Electrophoresis and Associated Microtechniques*, pp. 1085–1120. CRC Press.
- CHEN, C.-H., LIN, H., LELE, S. K. & SANTIAGO, J. G. 2005 Convective and absolute electrokinetic instability with conductivity gradients. *J. Fluid Mech.* **524**, 263–303.
- EVERAERTS, F. M., BECKERS, J. L. & VERHEGGEN, T. P. E. M. 1976 *Isotachophoresis: Theory, Instrumentation, and Applications*. Elsevier.
- GEBAUER, P., MALÁ, Z. & BOČEK, P. 2007 Recent progress in capillary ITP. *Electrophoresis* **28** (1–2), 26–32.
- GHOSAL, S. 2002 Band broadening in a microcapillary with a stepwise change in the zeta-potential. *Anal. Chem.* **74** (16), 4198–4203.

- HERR, A. E., MOLHO, J. I., SANTIAGO, J. G., MUNGAL, M. G., KENNY, T. W. & GARGUILO, M. G. 2000 Electroosmotic capillary flow with nonuniform zeta potential. *Anal. Chem.* **72** (5), 1053–1057.
- HIROKAWA, T., NISHINO, M., AOKI, N., KISO, Y., SAWAMOTO, Y., YAGI, T. & AKIYAMA, J. I. 1983 Table of isotachopheretic indices. I. Simulated qualitative and quantitative indices of 287 anionic substances in the range pH 3–10. *J. Chromatogr. A* **271** (2), D1–D106.
- JAROŠ, M., HRUŠKA, V., ŠTĚDRÝ, M., ZUSKOVÁ, I. & GAŠ, B. 2004 Eigenmobilities in background electrolytes for capillary zone electrophoresis. IV. Computer program peakmaster. *Electrophoresis* **25** (18–19), 3080–3085.
- JOVIN, T. M. 1973 Multiphasic zone electrophoresis. I. Steady-state moving-boundary systems formed by different electrolyte combinations. *Biochemistry* **12** (5), 871–879.
- KHURANA, T. K. & SANTIAGO, J. G. 2008 Sample zone dynamics in peak mode isotachopheresis. *Anal. Chem.* **80** (16), 6300–6307.
- KHURANA, T. K. & SANTIAGO, J. G. 2009 Effects of carbon dioxide on peak mode isotachopheresis: simultaneous preconcentration and separation. *Lab Chip* **9** (10), 1377–1384.
- KIRBY, B. J. & HASSELBRINK, E. F. 2004 Zeta potential of microfluidic substrates. 1. Theory, experimental techniques, and effects on separations. *Electrophoresis* **25** (2), 187–202.
- KOHLRAUSCH, F. 1897 Über concentrations-verschiebungen durch electrolyse im inneren von lösungen und lösungsgemischen. *Ann. Phys.* **298** (10), 209–239.
- KONSTANTINOV, B. P. & OSHURKOVA, O. V. 1966 Instrument for analyzing electrolyte solutions by ionic mobilities. *Sov. Phys.-Tech. Phys.* **11** (5), 693–704.
- LIN, H., STOREY, B. D., ODDY, M. H., CHEN, C.-H. & SANTIAGO, J. G. 2004 Instability of electrokinetic microchannel flows with conductivity gradients. *Phys. Fluids* **16** (6), 1922.
- MACÍNNES, D. A. & LONGSWORTH, L. G. 1932 Transference numbers by the method of moving boundaries. *Chem. Rev.* **11** (2), 171–230.
- MARTIN, A. J. P. & EVERAERTS, F. M. 1970 Displacement electrophoresis. *Proc. R. Soc. Lond. A* **316** (1527), 493–514.
- MARTIN, M. M. & LINDQVIST, L. 1975 The pH dependence of fluorescein fluorescence. *J. Lumin.* **10** (6), 381–390.
- MCHEDLOV-PETROSSYAN, N. O., KUKHTIK, V. I. & ALEKSEEVA, V. I. 1994 Ionization and tautomerism of fluorescein, rhodamine b, *n,n*-diethylrhodol and related dyes in mixed and nonaqueous solvents. *Dyes Pigment.* **24** (1), 11–35.
- PERSAT, A. & SANTIAGO, J. G. 2009 Electrokinetic control of sample splitting at a channel bifurcation using isotachopheresis. *New J. Phys.* **11** (7), 075026.
- PROBSTEIN, R. F. 1994 *Physicochemical Hydrodynamics: An Introduction*. Wiley-Interscience.
- SANTIAGO, J. G. 2001 Electroosmotic flows in microchannels with finite inertial and pressure forces. *Anal. Chem.* **73** (10), 2353–2365.
- SANTOS, J. J. & STOREY, B. D. 2008 Instability of electro-osmotic channel flow with streamwise conductivity gradients. *Phys. Rev. E* **78** (4), 46316.
- SAVILLE, D. A. 1990 The effects of electroosmosis on the structure of isotachopheresis boundaries. *Electrophoresis* **11** (11), 899–902.
- SAVILLE, D. A. & PALUSINSKI, O. A. 1986 Theory of electrophoretic separations. Part I. Formulation of a mathematical model. *AIChE J.* **32** (2), 207–214.
- SCHÖNFELD, F., GOET, G., BAIER, T. & HARDT, S. 2009 Transition zone dynamics in combined isotachopheretic and electro-osmotic transport. *Phys. Fluids* **21** (9), 092002.
- SHAKALISAVA, Y., POITEVIN, M., VIOVY, J. L. & DESCROIX, S. 2009 Versatile method for electroosmotic flow measurements in microchip electrophoresis. *J. Chromatogr. A* **1216** (6), 1030–1033.
- SOUNART, T. L. & BAYGENTS, J. C. 2007 Lubrication theory for electro-osmotic flow in a non-uniform electrolyte. *J. Fluid Mech.* **576**, 139–172.
- TAYLOR, G. 1953 Dispersion of soluble matter in solvent flowing slowly through a tube. *Proc. R. Soc. Lond. A* **219** (1137), 186–203.